Overview of HL-2A Experiment Results

Q.W.Yang 1), Yong Liu 1), X.T.Ding 1), L.W.Yan 1), D.Q.Liu 1), W.M.Xuan 1), L.Y.Chen 1), J.Rao 1), X.M.Song 1), Z.Cao 1), J.H.Zhang 1), X.R.Duan 1), W.C.Mao 1), C.P.Zhou 1), X.D.Li 1), S.J.Wang 1), M.N.Bu 1), Y.H.Chen 1), C.H.Cui 1), Z.Y.Cui 1), Z.C.Deng 1), J.Q.Dong 1), B.B.Feng 1), Q.D.Gao 1), W.Y.Hong 1), H.T.Hu 1), Y.Huang 1), Z.H.Kang 1), T.Lan 2), B.Li 1), G.S.Li 1), H.J.Li 1), Qiang Li 1), Qing Li 1), W.Li 1), Y.G.Li 1), Z.J.Li 1), Yi Liu 1), Z.T.Liu 1), C.W.Luo 1), X.H.Mao 1), Y.D.Pan 1), J.F.Peng 1), K.Shao 1), Z.B.Shi 1), X.Y.Song 1), A.K.Wang 1), H.Wang 1), M.X.Wang 1), Q.M.Wang 1), Y.Q.Wang 1), Z.G.Xiao 1), Y.F.Xie 1), L.H.Yao 1), L.Y.Yao 1), C.X.Yu 2), B.S.Yuan 1), K.J.Zhao 1), Y.Z.Zheng 1), G.W.Zhong 1), H.Y.Zhou 1), Y.Zhou 1), J.C.Yan 1) and C.H.Pan 1)

1) Southwestern Institute of Physics (SWIP), Chengdu, China
2) Department of modern Physics, Uni. of Science and Technology of China, Hefei, China.
E-mail of main contact author: yangqw@swip.ac.cn

Abstract: *The recent experiment results of the HL-2A tokamak are presented in this paper. Up to now, the stable and reproducible discharges with divertor configuration have been obtained, under the main plasma parameters of* $I_P = 400$ *kA,* $B_T = 2.65$ *T,* $N_e \sim 6.0\times10^{19}$ m^{-3} *and the discharge duration ~ 3.0 s, using the reliable feedback control. Siliconization is the normal wall conditioning method on HL-2A and after that, the impurity concentration and radiated power can be obviously suppressed after siliconization. Advanced scenario with weak positive/negative current shear, calculated by TRANSP codes using experimental data, is achieved by the central fuelling of the pellet injection. The supersonic molecular beam injection (SMBI) with liquid nitrogen temperature gas is used. It is proved that the low temperature SMBI can form the hydrogen cluster and penetrate into plasma more deeply and efficiently. The particle diffusion coefficient is obtained as* $0.5\sim1.5m^2/s$ *at plasma peripheral area. The symmetries (*$m = 0\sim1$*,* $n = 0$*) of the directly measured low frequency (7~9 kHz) electric potential and field are simultaneously observed for the first time by a novel designed Langmuir probe system. The impurity diffusion coefficient and convection velocity are determined by using laser blow-off system and transport code. In disruption studies, a new criterion for disruption prediction is given according to the MHD activity features and statistic analysis, and the plasma current quench time increases from about 5 ms to 20 ms with noble gas injection. The sawtooth character in on-axis ECRH experiment is investigated, and a persistent m=1 oscillation induced by SMBI and pellet injection is found to be a thermal fluctuation instead of magnetic island. The detachment characteristics of HL-2A divertor are numerically and experimentally studied using code SOLPS5.0 and measured data. The long divertor legs and thin divertor throats in HL-2A pose MHD shaping problems resulting in momentum losses even at low densities and strongly enhanced main chamber losses.*

Introduction:

Since the last IAEA fusion energy conference in 2004 [1], the plasma parameters of the HL-2A tokamak have been increased significantly with the improvement of the hardware of the device. The stable and reproducible discharges with divertor configuration have been obtained by the feedback control and wall conditioning techniques. Up to now, the main plasma parameters of HL-2A tokamak have reached $I_P = 400$ kA, $B_T = 2.65$ T, $\langle n_{e0}\rangle \sim 6.0\times10^{19}$ m^{-3} and the discharge duration ~ 3.0 s. The mission of HL-2A in this period is to improve the hardware, realize good performance and explore physics issues which include confinement improvement, divertor and scrape-off layer physics, wall conditioning, MHD instability and transport, auxiliary heating and current drive, etc.

Following section gives the experiment arrangements including the auxillary heating systems, diagnostics, fuelling systems, wall and wall conditioning method. Section 3 describes divertor discharge, high density operation and pellet enhanced performance (PEP) mode scenario on HL-2A. Section 4 presents the physics studies including particle transport, SMBI, impurity, disruption, turbulence and zonal flows, MHD instability and divertor.

Experiment conditions:

The experiment arrangements of HL-2A tokamak are illustrated in Fig.1. The total power of 3.0 MW auxillary heating system (including ECRH/ECCD and LHCD systems) and about 30 diagnostics are employed in experiments. In addition, the NBI system with the power of 1.5 MW is under installation.

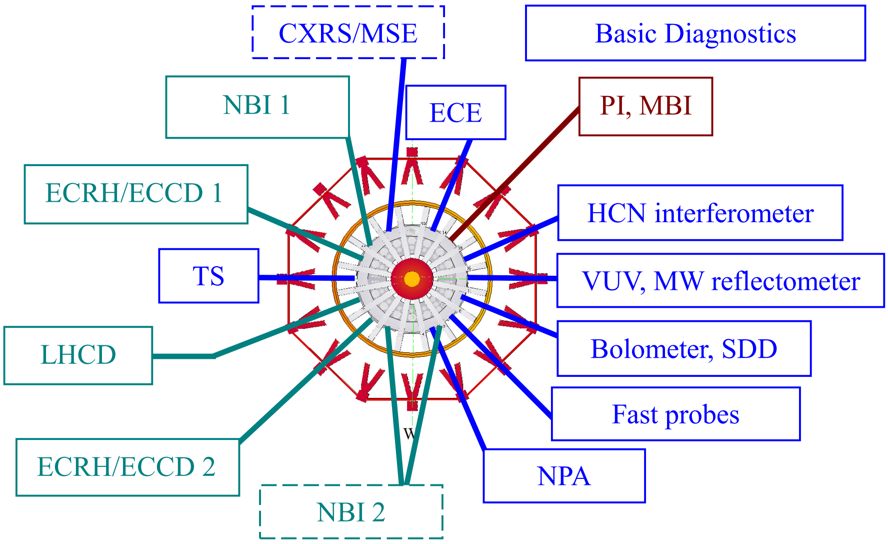

Fig.1 Illustration of HL-2A experiment arrangement in top-view.

The total power of 2 MW ECRH/ECCD system is mounted to two equatorial ports of device. Every port contains two transmission lines that transit the microwave power from 2 gyrotrons to plasma respectively. The power of each gyrotron is 500 kW, frequency is 68 GHz and pulse duration is about 1 second. The fundamental O-mode EC wave is chosen for resonant heating and current drive on HL-2A. The changes of power deposited position can be adjusted by steering the antenna poloidally and toroidally. The adjustable angles in poloidal and toroidal direction are 27° and 25°, respectively. LHCD system consists of 2 klystrons and a launcher with $N_{//} \sim 2.4$. Each klystron can provide 500 kW power (totally, 1 MW). Its frequency is 2.45 GHz and pulse length is about 1 second.

A NBI system with power of 1.5 MW, energy of 50 keV and pulse length of 2 s, which is named of NBI 1 in Fig.1, is under installation. Another NBI beam line (NBI 2) that has the same parameters with NBI 1 will be mounted in the opposite position of HL-2A, and will realize co-/count- injection.

About 30 diagnostics are equipped in HL-2A experiments. Besides some basic diagnostics such as magnetics, visible optics, fast ionization gauges, VUV spectrometer, divertor target probes, etc., a lot of advanced diagnostic systems with good temporal and spatial resolutions are developed on HL-2A. The 8-channel HCN interferometer [2] and scanning frequency (26 – 60 GHz) microwave reflectometer [2, 3] are used for electron density profile measurements and particle transport studies. The ECE radiometer, Thomson scattering and multi-channel soft x-ray spectrometer with SDD detectors are employed for electron temperature profile measurements. Neutral particle analyzer is for ion temperature detection. Three detector arrays, including soft x-ray [4] (with 5 arrays, 100 Channels), H-alpha (with 2 poloidal arrays and a tangential array) and bolometer [5] (4 arrays, 64 channels), are also installed on the device. After the tomography analysis the profiles of the soft x-ray intensity, H-alpha and thermal radiation can be obtained with good spatial resolution. The movable Langmuir probe arrays [6, 7], which are mounted to the equatorial ports in different toroidal position, are for plasma edge parameter, turbulence and zonal flows investigations.

The data acquisition system totally has about 1200 channels, and the maximum raw data volume in one shot is about 600 MB. According to the different needs of plasma parameter acquisition, the ADC sample rate can be selected from 10 kHz to 60 MHz.

The fuelling systems include direct gas puffing, pellet injector (PI) with velocity of 200 ~ 1400 m/s and the molecular beam injection [8, 9] (SMBI) with gas pressure of 0.2~3.0 MPa. Especially, the low temperature (liquid nitrogen temperature) SMBI is used. It is thought that the low temperature SMBI can form the hydrogen cluster more easily, and therefore can penetrate into plasma more deeply and efficiently [10].

To protect the components from plasma bombardment, divertor dome and buffer are covered by graphite and carbon fiber composite (CFC). The coverage of tiles is about 30% of the area facing the plasma.

Siliconization [11], based on the chemical vapor deposition by the GDC system with gas mixture of 90%He+10%SiH_4, is the most used method for wall conditioning on HL-2A. The typical parameters are: the gas pressure in the vacuum vessel is 8.8×10^{-2} Pa, the anode voltage is 650V and current is 2.4A. The current density on the surface of the first wall is about 5.3 $\mu A/cm^{-2}$. The impurity concentration and radiated power from plasma can be found decrease obviously after siliconization. Local deposition of silicon during plasma discharges by silane gas puffing is adapted. The results of the subsequent discharges show a similar effect on the plasma performance with normal siliconization.

Performance:

Divertor operation: The lower single null (LSN) divertor configuration has been achieved and sustained on HL-2A in 2003 [12]. After the improvements and optimizations of control system and algorithm, the stable and reliable divertor discharge can be easily obtained and usually covers the plasma current plateau and even the current ramp-down phase, as presented in Fig.2.

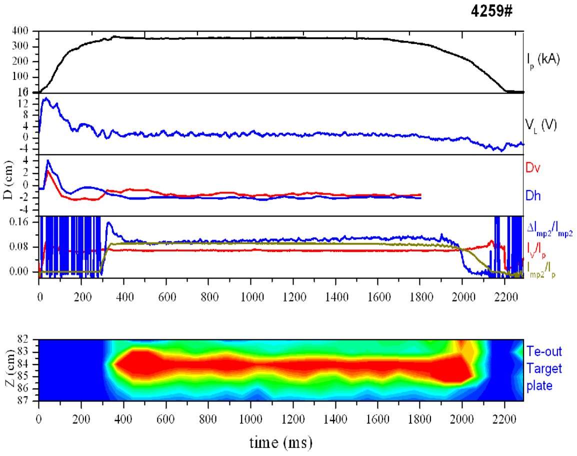

Fig.2 Divertor configuration sustainment

When the plasma displacements (3rd frame in

Fig.2) and the current in the multi-pole coils (4th frame in Fig.2) are controlled in the suitable value, divertor configuration can be formed and sustained. The image (bottom frame in Fig.2) implies the electron temperature profile on the divertor target plate. The red and blue regions respectively present higher and lower electron temperature detected by local Langmuir probe arrays.

High density discharges [13]: By direct gas puffing and SMBI, high density plasma discharges which approach/exceed the Greenwald limit are realized on HL-2A. In the experiment, firstly, the plasma current rises to the plateau. In this case plasma density almost keeps a constant. Then the plasma density increases. The discharge trajectories are marked in the Hugill diagram, as presented in Fig.3. The trajectories in red and orange (shot:03038 and shot:03054) are stopped in the “star” symbols on Hugill diagram that present the disruptions. The “star” symbols are very close to the Greenwald limit, which implies that they are density limit disruptions. The blue and cyan traces (shot:03037 and shot:03039) present the evolutions of disruption free discharges. The solid circles imply that the highest plasma densities are reached in the plasma current plateaus (i.e. in the maximum plasma current of each shot). In the plasma current ramping down phase, the plasma density increases continually. In this case, the Greenwald limit can be easily exceeded.

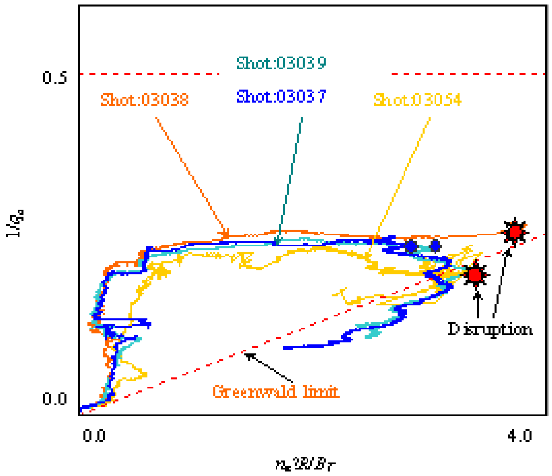

Fig.3 Discharge trajectories on the Hugill diagram. The solid symbols “☼” denote the place of disruption occurrence, and the symbols “●” indicate disruption free discharges.

PEP mode [14]: Enhanced confinement is achieved by the PI. After the pellets (typically, the third pellet at 710 ms in this shot) are injected in the plasma, the peaked factor of density $n_{e0}/n_{e(r/a=0.7)}$ increases from 1.55 (before the PI) to 3.1 (just after the 3rd PI), and the hollow temperature profile appears, which sustains about 200 ms (in the 3rd frame in Fig.4), but the improved confinement keeps about 500 ms. The poloidal β_p and the energy confinement time τ_E measured by diamagnetic probe gradually increase from 0.3 and 50 ms to 0.6 and 130 ms respectively after the PI, as shown in the 5th frame of Fig.4.

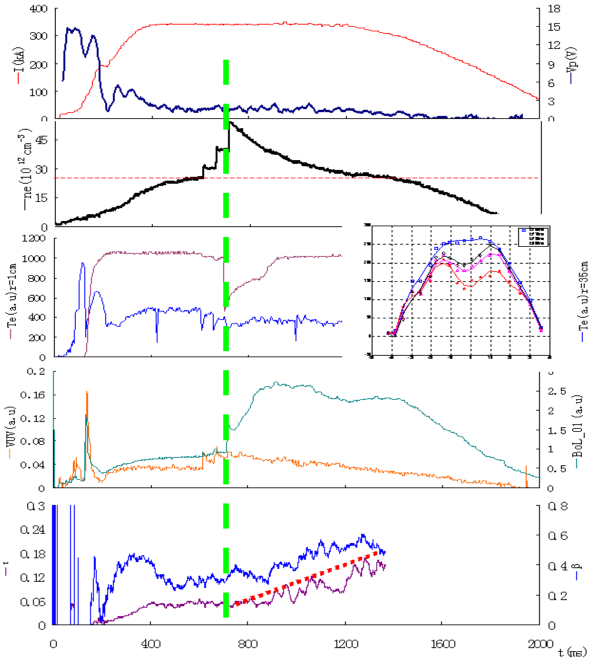

Fig.4 Typical waveforms of PEP mode

Experimental results show that the confinement improvement is related to the decrease of the electron heat transport. In fact, the electron heat diffusion coefficient χ_e in the plasma confinement region (r/a~0.5) decreases from about 6 m^2/s to about 2 m^2/s gradually after PI. Correspondingly, two phases with different T_e/T_i in this period are found: $T_e/T_i \sim 1$ at 710 – 850 ms increases to $T_e/T_i > 1.5$ at 850 – 1200 ms.

The weak positive/negative magnetic shear, calculated by TRANSP codes using experimental data (shown in Fig.5), is thought to be a key cause for the decrease of T_e/T_i and low electron heat transport.

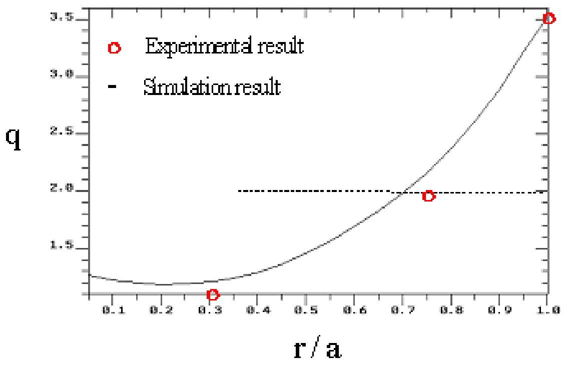

Fig.5 q profile after the pellet injection.

Physics studies:

SMBI fuelling [10]: The SMBI, a more efficient and deeper fuelling method than normal gas puffing, has been investigated in last decade. The depth of SMBI is experimentally studied using modulated SMBI on HL-2A in recent campaigns.

Asymmetric cold pulse perturbation is observed in low density ($\sim 1\times10^{19}$m^{-3}) by means of electron–cyclotron emission (ECE) and soft-x-ray array during pulse-modulated molecular beam injection (SMBI) experiments [15]. The perturbation depth is about 30 cm from the low field side (LFS) and only about 10 cm from the high field side (HFS), when the molecular beam is injected into plasma from LFS. The cold pulses cannot propagate to the plasma center from either the low or high field side. The electron temperature in the plasma center does not change during SMBI, but electron density pulse perturbations can be observed in the plasma center from the ECE 3rd harmonic measurements, which corresponds to the results of the far-infra-red laser interferometer. The experimental results indirectly provide evidence of the shielding mechanism of the SMBI physics.

The results, obtained from the experiment using microwave reflectometer and modulated SMBI, confirm that pulsed SMBI is a good perturbation source with deeper penetration and better localization than the general gas puffing. After FFT analysis, the amplitude and the phase profiles of the modulated SMBI pulse propagation show that the particle source injected by pulsed SMBI is located at about r/a = 0.5 ~ 0.75, where the obvious minimum phases can be observed, as shown in Fig.6.

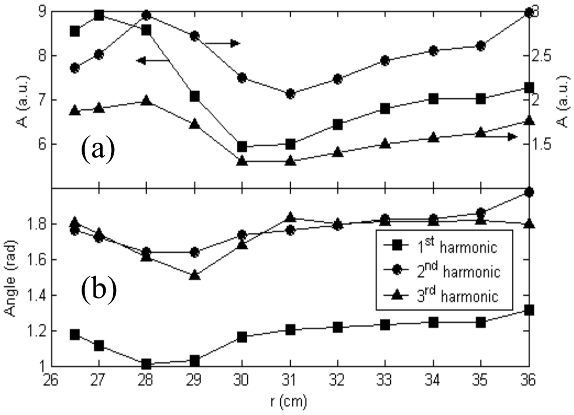

Fig.6 FFT analysis of the modulated MBI pulse. (a) and (b) are the amplitude "*A*" and phase "*Φ*" profiles of first "■", second "▲" and third "●" harmonic, respectively.

It is found that the injection depth of SMBI is in dependent upon some parameters, such as plasma temperature, density and the pressure of the injected gas. On HL-2A, the relationship between the injection depth of SMBI and some parameters is investigated experimentally. An empirical scaling is given as:

$$d = C \cdot \overline{N}_e^{-0.2} \cdot \overline{T}_e^{-0.6} \cdot P^{0.3}$$

here, d is the injection depth normalized by minor radius, $\overline{N}_e$ is the average plasma density ($\times 10^{19}$m^{-3}), $\overline{T}_e$ is the average electron temperature (keV), P is the pressure of injected gas (MPa), C=0.35, is a coefficient related to the parameters of nozzle geometry and temperature of working gas. This scaling is in good agreement with the experiment data, as shown in Fig.7.

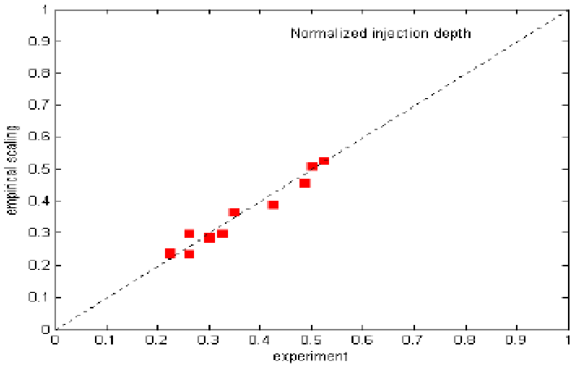

Fig.7 Comparison of MBI depth between experimental data and empirical scaling on HL-2A.

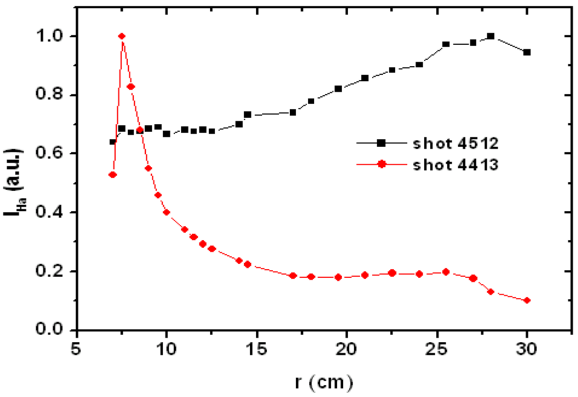

Fig.8 Profiles of Hα emission measured by the tangential detector array for shot 4413 (LNT) and 4512 (RT).

The hydrogen cluster jet can be obtained when the working gas is decreased to liquid nitrogen temperature (LNT) and the gas pressure is over 1.0 MPa. The results show that the low temperature SMBI can penetrate into plasma deeper than room temperature (RT) one, See Fig.8.

Particle transport: Using microwave reflectometer and modulated SMBI, the particle transport is investigated on HL-2A as well. In Fig.6, The maximum amplitude of the first harmonic shifts inward, indicating the presence of an inward convective component. For the second and third harmonic, this feature disappears and a standard diffusive pattern can be found. Therefore, we can obtain the diffusion coefficient:

$$\lambda_d = (2D/\omega)^{1/2}$$

$$V_\Phi = (2\omega D)^{1/2} \quad \text{and} \quad D = \omega / 2(\Phi')^2$$

here, D is diffusion coefficient, ω is harmonic frequency, Φ is the phase, λ_d is the characteristic length of the amplitude decays, V_Φ is the and phase velocity. Fig.9 shows the diffusion coefficient profile calculated by the above formula. The particle diffusion coefficient during an Ohmic discharge is about 0.5~1.5m^2/s at r/a = 0.5 ~ 0.75, which is about 1/4 of the electron heat diffusivity. The data in the area of r > 30 cm in Fig.9, may have great error because of the effect of the edge particle source.

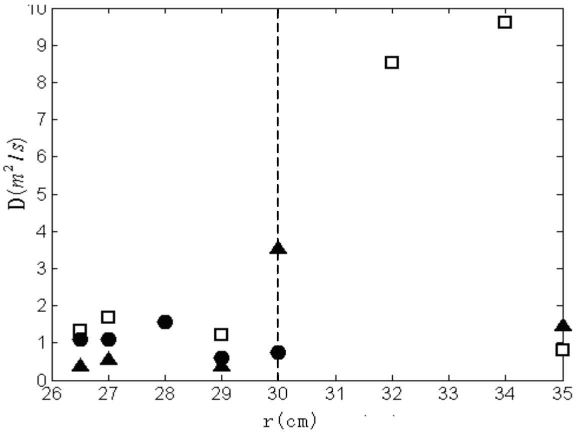

Fig.9 Profile of particle diffusion coefficient. ▲-first harmonic, □-second harmonic, ●-third harmonic.

Zonal Flows [16, 17]**:** Three-dimensional features of geodesic acoustic mode (GAM) zonal flows (ZFs) are determined with 3-step Langmuir probes [6] at the edge of the plasmas. The symmetries (m ≈ 0~1, n ≈ 0) of the directly measured low frequency (7~9 kHz) electric potential and field are simultaneously observed for the first time. The radial scale length of the flows is estimated as 2.4~4.2 cm. The formation mechanism of the flows is identified to be nonlinear three-wave coupling between high frequency turbulent fluctuations and the flows.

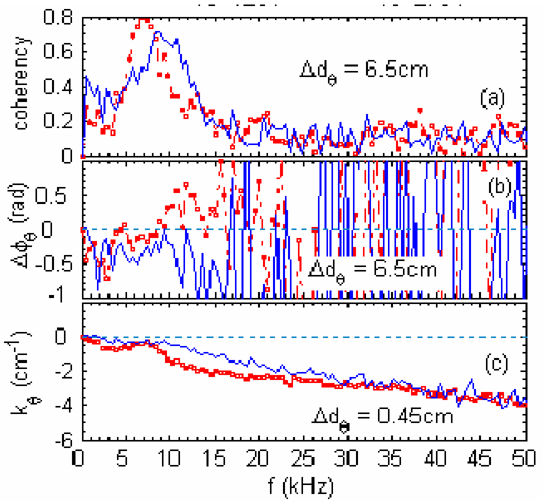

Fig.10 Coherency spectrum of the radial electric field strength E_{r1} and E_{r2} (a), the corresponding phase difference $\Delta\varphi_\theta$ (b) and wave vector spectrum k_θ calculated from φ_{f1} and φ_{f3} (c).

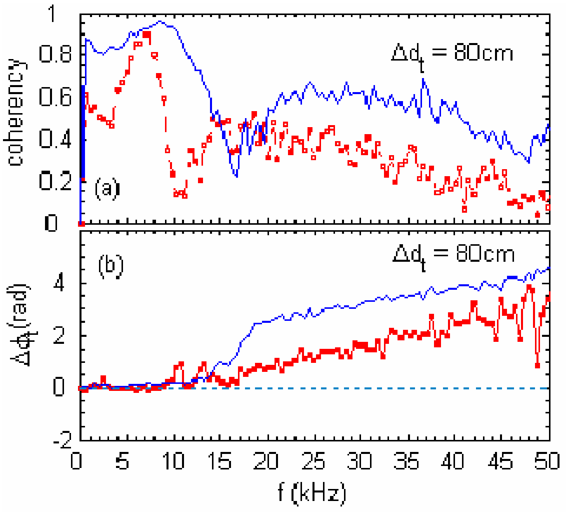

Fig.11 Coherency spectrum of the radial electric field strength E_{r1} and E_{r2} (a), and the corresponding phase difference $\Delta\varphi_t$ (b).

Shown in Fig.10 are (a) coherency spectra of E_{r1} and E_{r2}, which are the radial electric field component of the at two poloidal positions with a separation of 6.5 cm, (b) the phase difference $\Delta\varphi_\theta$ between E_{r1} and E_{r2}. The coherencies at the peak frequencies of the auto power spectra are 0.7 and 0.79, indicating a strong correlation over the 65mm distance in the poloidal direction. The long poloidal wavelength feature of the geodesic acoustic mode flow is also demonstrated by the near zero phase shift of the oscillations in the frequency region over the distance. The poloidal wave vector k_θ versus frequency f estimated from Φ_{f2} and Φ_{f3} is given in Fig.3(c) where a general dispersion relation without an offset for the ambient turbulent (AT) and a deviation in the GAM frequency region are clearly illustrated. The poloidal wave vector $k_\theta = -0.02\pm0.01$ cm^{-1} and -0.05 ± 0.03 cm^{-1} are calculated form E_{r1} and E_{r2}. The mode number m~0 is estimated for the GAM zonal flows (ZF).

Fig.11 describes the toroidal structure of the radial component of the electric field. Given here are (a) the coherency spectra of E_{r1} and E_{r3}, which are the radial electric field at different toroidal positions with a separation of 80 cm, (b) phase difference $\Delta\varphi_t$ between E_{r1} and E_{r3}. The coherent structure of the GAM frequency oscillations over the 800mm distance in the toroidal direction is clearly illustrated by the coherencies of 0.9 and 0.96. The sharp decrease

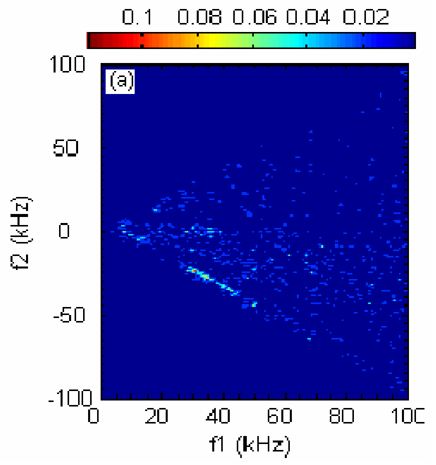

Fig.12 Bicoherence $b^2(f_3)$ in f_1-f_2 plane

of the phase shift in the GAM frequency region distinguishes the GAM ZF from the AT. The calculated toroidal wave vectors are $k_\varphi = (0.02\pm0.07)\times10^{-2}$ cm^{-1} and $(0.22\pm0.04)\times10^{-2}$ cm^{-1}, respectively. The toroidal mode numbers n ~0 is calculated for the GAM ZF.

As for the generation mechanism of the GAM ZFs, the squared cross-bicoherence, $b^2(f_3)=|B(f_3)|^2/[<|v_r(f_1)v_\theta(f_2)|^2><|v_\theta(f_2)|^2>]$, of the perturbation is calculated. This is an indicator for the strength of nonlinear three wave coupling. Here, the bispectrum, $B(f_3)=<v_r(f_1)v_\theta(f_2)v_\theta^*(f_3=f_1+f_2)>$. Fig.12 shows $b^2(f_3)$ plotted in the f_1-f_2 plane. The values of $b^2(f_3)$ about $f_3=f_1-|f_2|\sim7$kHz are higher than that at the rest frequencies, indicating that the GAM ZFs are created by nonlinear three wave coupling. The frequency resolution is 1kHz in this analysis and signals are significantly above the noise level of 0.005 in the wide range of frequency.

In addition, the physical mechanism for the generation of the observed GAM ZFs is under investigation and the influences of the GAM ZFs on the ATs are explored in detail. The results are compared with the theoretical predictions.

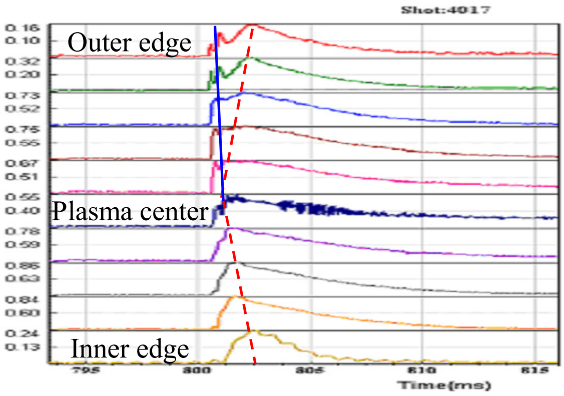

Fig.13 Bolometer signals during impurity injection.

Impurity [18, 19]: Small quantities of medium-Z impurities (Titanium and Aluminium) were injected into HL-2A plasmas by laser blow-off (LBO) to study impurity transport. Using the bolometer cameras, which are useful for observing the behaviors of the injected impurity in plasma periphery, and soft X-ray cameras, which are contributed to that in plasma center, the whole inward and outward movements of the injected impurity are clearly obtained, as shown in Fig.13. In the very early time and in the outside region of plasma the injected impurity ions have asymmetric profile, presented as the solid blue line in Fig.13. Then they propagate from the plasma center to edge with the symmetric distribution, presented as the dashed red line in Fig.13.

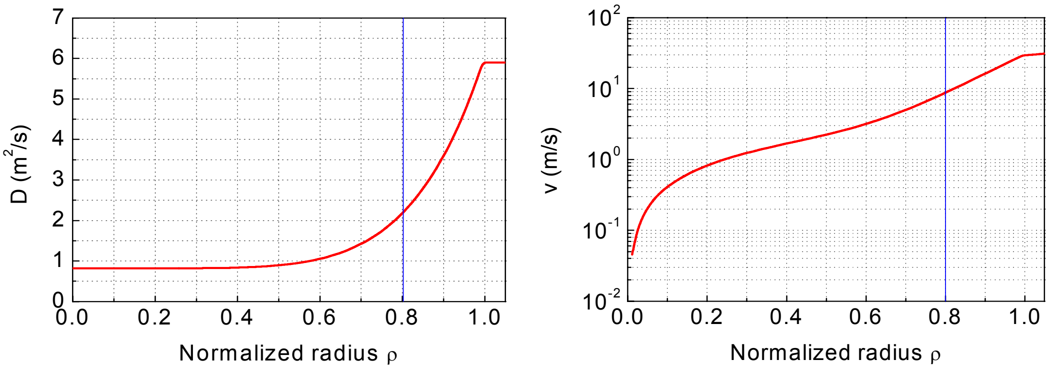

Fig.14 The profiles of the diffusion coefficient *D* and convection velocity *V* on HL-2A shot:04057.

Using a 1-D impurity transport code and experiment data by VUV spectrometer, soft X ray arrays, and Bolometer arrays, the diffusion coefficient *D* and convection velocity *V* have been determined primarily on HL-2A. In the central of plasma ($0 \leq \rho < 0.5$), the typical values of *D* and *V* are 0.5 – 1.0 m^2/s and < 2.0 m/s, respectively. However, in the range of $0.5 \leq \rho < 0.8$, the values are 1.0 – 2.5 m^2/s and 2.0 – 10.0 m/s, see Fig.14. They are much larger than those of the neoclassical theory predictions, and impurity transport is anomalous. The anomalous behavior of impurity transport will be deeply researched on theory and experiment.

Disruption[20, 21]: The statistical analysis implies that more than 60% of the plasma current quench time is in the region of 4 - 6 ms in HL-2A major disruptions (given in Fig.15). It indicates that the major disruptions are fast disruption. A simple model is employed to estimate the dependence relation between dI_P/dt during current quench and loop voltage, which is presented in Fig.16, by a solid red curve. The simulative result is in agreement with the experiments data, which is marked with solid triangles.

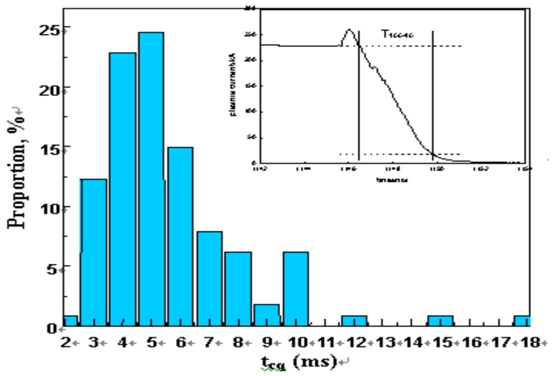

Fig.15 Statistic of current quench time in HL-2A major disruption.

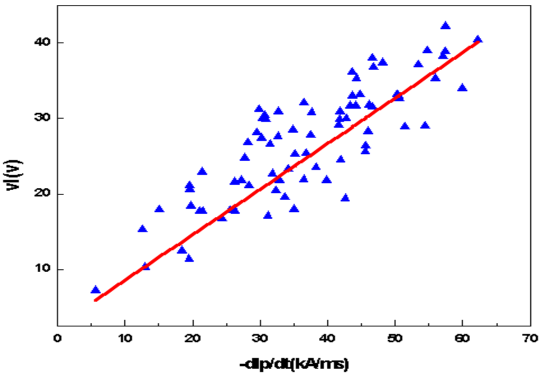

Fig.16 Comparison between the simulation and experiment.

The major disruption features and its relationships with the plasma parameters are studied. It is found that MHD activity is always observed before the disruption. The large MHD perturbations, especially, the locked m = 2 mode, can be used as disruption precursor to predict the major disruption. Thereby, based on the statistic analysis of the MHD perturbation, a new criterion, $\int \tilde{B}_\theta \cdot dt$, for disruption prediction is introduced. Here, $\tilde{B}_\theta$ is the poloidal perturbation signal obtained by Mirnov coil. The physics meaning of $\int \tilde{B}_\theta \cdot dt$ is the amplitude multiplies the period of MHD fluctuation.

A prediction system for disruptions is developed in the HL-2A tokamak, which consists of an artificial neural network, fed by the diagnostics signals. The best network configuration is composed of 13 inputs, three hidden layers with 15, 30, 10 hidden neurons, respectively, and 1 output. 13 diagnostics signals are taken as the inputs. 1 or 0 is taken as the output, which means the stability and disruption, respectively. The trained network has successfully forecasted the disruptive events in the test sets, up to 20ms in advance. The results show that the network can be installed to work on line as part of the control system of HL-2A tokamak in the future.

The disruption mitigation has been demonstrated by noble gas (Neon and Argon) puffing. The huge radiation loss during noble gas injecting can successfully increase the quench time and decrease the runaways during major disruption. Comparing the current quench time is about 5 ms in HL-2A major disruption, it can be increased to greater than 20 ms with the mitigation adopted.

MHD instability [22]**:** During on-axis ECRH, a strong m = 1 mode is excited at q = 1 surface. Comparing the sawteeth in Ohmic discharge, the precursor oscillation in ECRH plasma is much large. With the strong m = 1 oscillation driven by ECRH, a sawtooth tends to saturate, as shown in fig.17. It is thought that this strong m = 1 mode is the main reason for the formation of the saturated sawtooth. Furthermore, the on-axis ECRH can cause the period of the sawtooth to decrease (in the bottom frame of Fig.17). It suggests that the centrally localized electron cyclotron heating increases the central plasma temperature. Hence it increases the current penetration time over the central region in the sawtooth ramp phase and leads to sawteeth with smaller periods.

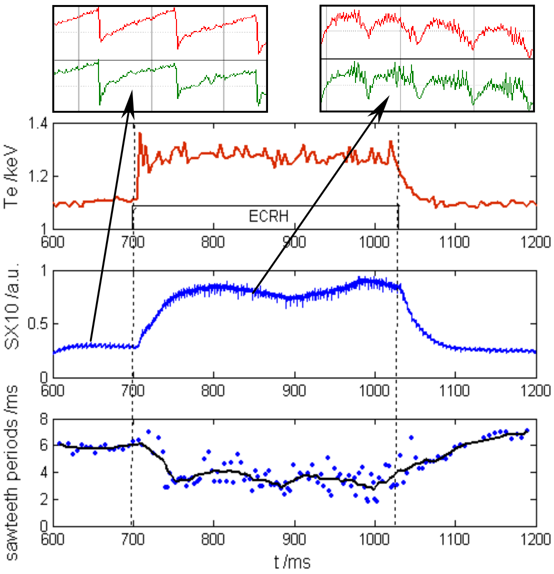

Fig.17 Characters of sawteeth during ECRH experiments

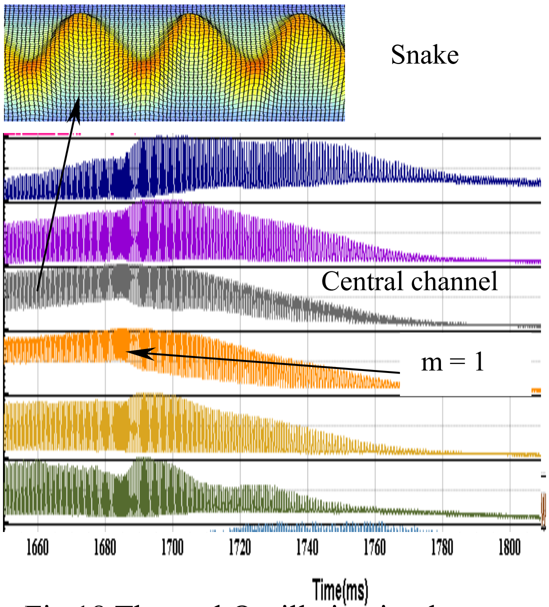

Fig.18 Thermal Oscillation in plasma core after PI

A large, persistent and sawteeth absent m = 1 perturbation has been observed in the core region after PI on the HL-2A plasma by soft x ray array. After singular value decomposition (SVD) analysis, it can be determined that this perturbation has typical snake phenomenon, as shown in Fig.18. In the SMBI case, due to the large number of neutrals in a high-pressure supersonic gas jet, and the low parameters of the incident electrons which are determined by the relatively low parameters of the HL-2A plasma (especilly the density and temperture), the ionization degree and temperature in the whole jet volume are quite low. This may help the jet to penetrate into the core region of the plasma, and cause the formation of a persistent m =1 oscillation.

Divertor [23]**:** Numerical analysis of HL-2A divertor discharges is done using two dimensional multi-fluid edge code SOLPS5.0. The detachment characteristics are determined under the specific divertor geometry. According to the simulation results, when the electron density at core interface boundary (CIB) is rather low ($n_e \leq 0.5\times10^{19}\mathrm{m}^{-3}$ in single null which is HL-2A configuration), the maximum electron densities in the inner/outer divertor targets rise linearly with the density at the CIB. When the density at the CIB reaches intermediate values ($0.5\times10^{19}\mathrm{m}^{-3} \leq n_e \leq 2\times10^{19}\mathrm{m}^{-3}$ in single null configuration), the difference between the maximum electron density at target plate and the mid-plane density becomes larger and then the maximum density approaches the mid-plane density while the electron temperature at the target decreases to 5eV. This is not a local high recycling regime with large flux amplifications and much higher density at target plate than that at midplane. This results in momentum losses already at low densities from the interaction of the streaming divertor plasma with this neutral cushion. Therefore, a strong deviation from the common 2-point scaling is observed if local parameters are used, similar to island divertors in stellarators. The thin divertor throats in HL-2A pose MHD shaping problems resulting in strongly enhanced main chamber losses, because a large amount of the power is lost at baffles and does not even get into the divertor.

The phenomenon similar to the partially detached divertor regime is observed on HL-2A experiment with electron density of $1.5\times10^{19}m^{-3}$ in main plasma [24]. After a strong gas puffing the electron temperature measured on the outer divertor target plate near the separatrix decreases till below 5 eV or even lower, but that of the farther outer divertor target plate does not change obviously; the CIII and Hα emission at the plasma edge decrease as expected, but the Hα emission near the X-point increases.

Based on the surface temperature measured by the infrared camera and the one dimension heat conduct model, the deposited power density on the divertor plate is determined as 100-200 kW/m^2 in HL-2A Ohmic discharges. It means that the deposited power density remains small. The typical waveforms of power deposition are presented in Fig. 19 in which the Ohmic power is about 550kW and the average line electron density is about 2×10^{19}m-^{3}.

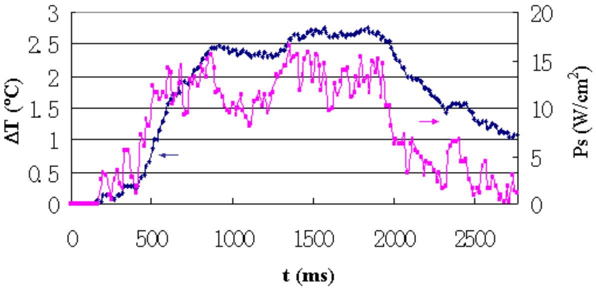

Fig.19 The surface temperature and deposited power density on outer divertor target plate Z=-86.5cm.

Summary and discussion:

On HL-2A, the Ohmic plasma can be stably and reliably operated in lower single null divertor configuration, and reaches parameters of plasma current $I_P = 400$ kA, toroidal magnetic field $B_T = 2.65$ T, line-average density $N_e \sim 6.0\times10^{19}\ m^{-3}$ and the discharge duration ~ 3.0 second. The ability of auxillary heating is about 4.5 MW, which includes ECRH/ECCD (2 MW), LHCD (1 MW) and NBI (1.5 MW, under installation).

Some experimental results have been obtained in recent HL-2A campaigns.

- The detailed investigations of SMBI have been carried out. The penetration distance of SMBI is much deeper in LFS than it is in HFS, which indicates that SMBI particles can be injected into plasma as the pellet injection being, instead of diffusing from plasma edge as the gas puffing case. A preliminary scaling of HL-2A is revealed for first time. Furthermore, the LNT SMBI can penetrate into plasma more deeply and efficiently. It is thought that it is because of the hydrogen cluster formed in low temperature condition, and the cluster is of benefit to particle penetration.
- Using microwave reflectometer and modulated SMBI, the particle transport is investigated. The particle diffusion coefficient is determined, which is about 0.5~1.5m^2/s in plasma peripheral region.
- Three-dimensional features of GAM ZFs are determined with novel designed 3-step Langmuir probes. The symmetries (m = 0~1, n = 0) of the directly measured low frequency (7~9 kHz) electric potential and field are simultaneously observed.
- The diffusion coefficient D and convection velocity V of impurity (Titanium and

Aluminium) are estimated primarily using LBO and a 1-D transport code. They are 0.5 – 1.0 m^2/s and < 2.0 m/s, respectively.

- According to the studies of MHD instability, a new criterion is introduced for disruption prediction. A primary off-line neural network is also developed on HL-2A. To mitigate the major disruption, the noble gas (Neon and Argon) injection are demonstrated and it can successfully increase the current quench time from about 5 ms, which is based on the statistic analysis, to greater than 20 ms when the major disruption occurs. Because the molecular beam can inject into plasma more deep, the disruption mitigation will be under the SMBI in future experiments.
- A large, persistent and sawteeth absent m = 1 perturbation is observed in the plasma core after SMBI and PI. The investigational results reveal that it is a thermal fluctuation instead of magnetic island. The more detailed studies will be carried out experimentally and therotically.
- The detached (or partially detached) divertor regime is easily occurrence, even in the intermediate density operation on the unique close divertor. The reason is considered to be the long divertor legs and the thin divertor throats. The numerical simulations are in good agreement with the experiments.

Reference:

[1] Yong Liu, X.T.Ding, Q.W.Yang, *et al.*, *Nuclear Fusion*, **45** (2005) S230.

[2] X.T.Ding, Y.Zhou, Z.C.Deng, *et al.*, *16th Annual Conference on High - Temperature Plasma Diagnostics 7-11 May 2006,* HTP2, *Williamsburg, VA, USA.* To be published in *Review of Scien. Instruments,* **Vol.77** (2006),

[3] W.W.Xiao, Z.T.Liu, X.T.Ding, *et al.*, *Plasma Scien. & Tech.,* **Vol.8** (2006), 133.

[4] Y.B.Dong, Yi Liu, L.H.Yao, *et al.*, *5th conf. of Asia Plas. & Fusion Association (APFA), Aug. 29-31, 2005, Jeju, Korea*. To be published in *J. Korean Physical Society*, 2006.

[5] Y.D.Pan, *et al.*, *33rd EPS Conf. on Plas. Phys.,* Jun. 17-23 2006, Rome, Italy, P2.174.

[6] L.W.Yan, W.Y.Hong, J.Qian, *et al.*, *Review of Scien. Instru.,* **Vol.76** (2005), 093506.

[7] L.W.Yan, W.Y.Hong, *et al.*, to be published in *Review of Scien. Instru.,* **Vol.77** (2006).

[8] L.H.Yao, *et al.*, *Nucl. Fusion,* **38** (1998), 631.

[9] L.H.Yao, *et al.*, *Nucl. Fusion,* **41** (2001), 817.

[10] L.H.Yao, B.B.Feng, C.Y.Chen, *et al.*, *this conf.*, EX/P3-21.

[11] X.R.Duan, Z,Cao, *et al*,. *17th Inter. Conf. on PSI*, May 22-26 2006, Hefei, China, O-26.

[12] Q.W.Yang, X.T.Ding, et al., *Chin. Phys. Lett.* **Vol.21** (2004) 2475.

[13] Q.W.Yang, *et al.*, *32nd EPS Conf. on Plas. Phys.,* June 27 - July 1 2005*, Tarragona, Spain,* P1.065.

[14] X.T.Ding, Q.W.Yang, *et al.*, *Chin. Phys. Lett.* **Vol.23** (2006), 2502.

[15] Z.B.Shi, X.T.Ding, L.H.Yao, *et al.*, *Plas. Phys. Control. Fusion* 47 (2005) 2019.

[16] K.J.Zhao, T.Lan, *et al.*, *Physical Review Letters,* **96** (2006), 255004

[17] L.W.Yan, W.Y.Hong, T.Lan, *et al.*, *this conf.*, EX/P4-35.

[18] Z.Y.Cui, Y.Huang, P.Sun, *et al.*, *Chin. Phys. Lett.* **Vol.23** (2006), 2143.

[19] Z.Y.Cui, *et al.*, *33rd EPS Conf. on Plas. Phys.,* Jun. 17-23 2006, Rome, Italy, P2.171.

[20] H.Y.Zhou, Q.W.Yang, *et al.*, *33rd EPS Conf. on Plas. Phys.*, Jun. 17-23 2006, Rome, Italy, P2.176

[21] Q.W.Yang, H.Y.Zhou, *et al.*, *Chin. Phys. Lett.* **Vol.23** (2006), No.4 P891.

[22] Yi Liu, Y.B.Dong, W. Deng, et al., *this conf.*, EX/P8-13.

[23] Y.D.Pan, R.Schneider, *17th Inter. Conf. on PSI*, May 22-26 2006, Hefei, China, P1-59.

[24] X.R.Duan, X.T.Ding, Q.W.Yang, *et al.*, *Plasma Scien. and Tech.*, **Vol.8** (2006), 19.